

# Harnessing Green Synthesized TiO<sub>2</sub> Nanoparticles From *Leucas indica* Extracts for Effective Antibacterial Action against Wound Pathogens

Neelesh Babu<sup>1,\*</sup> , Abhishek Bhardwaj<sup>2</sup> , Navneet<sup>3</sup> , Vishal Kamboj<sup>4</sup> 

<sup>1</sup> Department of Microbiology, SOAS, Dev Bhoomi Uttarakhand University, Dehradun-248007, India

<sup>2</sup> Department of Applied Physics, Delhi Technological University, Delhi-110042, India

<sup>3</sup> Department of Botany and Microbiology, Gurukula Kangri Vishwavidyalaya (Deemed to be University), Haridwar, Uttarakhand 249404, India

<sup>4</sup> Department of Environmental Science, BFIT Group of institutions, Dehradun-248007, India

\* Correspondence: sonkarneil@gmail.com;

Scopus Author ID: 57654702200

Received: 30.12.2023; Accepted: 7.07.2024; Published: 16.02.2025

**Abstract:** The green synthesized Titanium dioxide (TiO<sub>2</sub>) nanoparticles were examined for their antibacterial efficacy against five bacterial isolates (Isolate B, C, D, E, and G) from the wound infection site. These isolates were biochemically analyzed using Hi-Medial kits KB003 and KB009, followed by molecular characterization by 16S rRNA sequencing. The Isolates B, C, and D were identified as *Staphylococcus aureus*, whereas Isolate E was *Pseudomonas aeruginosa* and Isolate G was *Escherichia coli*. The results obtained from the antibacterial efficacy of green synthesized nanoparticles revealed that these nanoparticles actively inhibited all the bacterial isolates. *Pseudomonas aeruginosa* strain E was most sensitive against all the nanoparticles, whereas *Escherichia coli* strain G was least sensitive. The bactericidal ability could be attributed to how ROS (reactive oxygen species) interacts with lipid membranes, ultimately resulting in the peroxidation of lipids and subsequent cell membrane rupture, causing the cell's death. Reactive oxygen species (ROS) production could be linked to the effectiveness of hydroxyl radical (OH) generation within the anatase phase of TiO<sub>2</sub> nanoparticles. Upon interacting with the cell, highly reactive OH radicals are produced by the anatase phase of titanium dioxide nanoparticles. This is why they have a brief lifespan, from the moment they are produced. They immediately interact with the outer surface of the bacteria until the titanium dioxide particles penetrate the cell.

**Keywords:** titanium dioxide; green synthesis; nanoparticles; *Leucas indica*; antibacterial efficacy; isolation; reactive oxygen species.

**Abbreviations:** TiO<sub>2</sub>/PE: nanoparticles synthesized via a green synthesis utilizing petroleum ether extract; TiO<sub>2</sub>/BZ: nanoparticles synthesized via a green synthesis utilizing benzene extract; TiO<sub>2</sub>/MeOH: nanoparticles synthesized via a green synthesis utilizing methanol extract; TiO<sub>2</sub>/W: nanoparticles synthesized via a green synthesis utilizing water extract; DW: Distilled water; Amp: Ampicillin; Cfz: Cefazolin; Str: Streptomycin.

© 2025 by the authors. This article is an open-access article distributed under the terms and conditions of the Creative Commons Attribution (CC BY) license (<https://creativecommons.org/licenses/by/4.0/>).

## 1. Introduction

Titanium dioxide, known as titania, belongs to the transition metal oxide family with the chemical formula TiO<sub>2</sub> [1]. Titanium dioxide has been considered one of the most appropriate semiconducting materials with a wide scope of mechanical applications, such as

photocatalysts. It is very cost-effective and has a high surface-to-volume ratio, and its non-poisonous property makes it the most suitable material [2]. Titanium dioxide (TiO<sub>2</sub>) nanoparticles have many applications due to their high photo-stability, oxidation strength, and negligible toxicity [3]. It is used in cosmetics such as sunscreens to protect skin from ultraviolet rays [4]. It also has various applications in the field of photocatalysis, gas sensors, water treatment, solar cells, photoelectrochemical cells, and protective coatings on optical elements [5]. It is widely used in paints, coatings, plastics, papers, inks, foods, medicines, and toothpaste [6]. The chemical synthesis of nanoparticles, such as solvothermal reduction, chemical reduction, and electrochemical reduction, is costlier, toxic, difficult to separate, hazardous, and employs high pressure and energy [7]. Besides these, green synthesis of nanoparticles has been adopted as an alternate method that utilizes biological materials such as plant crude extract as reducing agents [8]. Phytochemicals in the crude extracts of plants act as capping agents in the green synthesis of nanoparticles. A synergetic effect will be provided when the particles are coated with phytophenolic compounds of the crude extracts utilized in the biomedical field [9]. Although several methods, such as the thermal decomposition method, hydrothermal and solvothermal method, microwave-assisted method, polyol method, sonochemical method, liquid-liquid interface method, phase-transfer method, biosynthesis method, template-directed synthetic method, etc., are there for the nanomaterial synthesis for the present study sol-gel procedure is considered because of it has ability to control the surface properties and texture of the material, stoichiometry, of the precursors, tailorable microstructure, relatively low annealing temperature, utilizes inexpensive and simple apparatus [10,11].

The extensive exploitation of antibiotics leads to several drug-resistant bacteria causing delayed healing or much worse circumstances. So, there is a need to develop certain novel kinds of medications under such conditions. The main focus of the study is to prepare an alternative medication or compound that can be used with conventional medicine against wound infection-causing pathogens. For the present study, extracts of the herb *Leucas indica* were utilized to prepare TiO<sub>2</sub> nanoparticles as it is widely utilized for wound healing and treating wound infection. The botanical name of Guma, Tumba, or Dandokalos is *Leucas indica*, which falls under the Lamiaceae family. It can be found throughout India, mainly in roadside wastelands, riverbanks, and rocky hills. This plant is characterized by its pubescent branching and erect herb structure. Its leaves are long and narrow, while its flowers have four stamens and are white. In the Garhwal region of Uttarakhand, it has been traditionally used as a remedy for treating wounds. The leaves of this plant are squeezed and placed on wounds to obtain wound healing [12]. Extensive research has been conducted on the chemical components of this plant. Chemical analysis of various parts of the plant showed the presence of carbohydrates, alkaloids, steroids, flavonoids, triterpenoids, fatty alcohol, etc. [13].

## 2. Method and Materials

### 2.1. Preparation of TiO<sub>2</sub>.

Titanium dioxide nanoparticles were synthesized by employing the sol-gel technique, utilizing titanium isopropoxide (Sigma Aldrich >97%) as the titanium precursor. As per the method demonstrated by Liu *et al.*, (2003), preparation was accomplished with some modifications [14]. To initiate the synthesis, 10 mL of ethanol was used to suspend four separate extracts, then individually mixed with 5 mL of Titanium isopropoxide. Under vigorous stirring at room temperature for 12 hours, each suspension was slowly added dropwise to a

solution containing ethanol, HCl, and deionized water (in a ratio of 30:1.66:1). The resulting solutions were further precipitated and subjected to recovery by centrifugation under ethanol medium. The resulting precipitate was subjected to a drying process at a temperature of 70°C, followed by annealing in a muffle furnace at 500°C [14]. The herb *Leucas indica* was collected from the prominent town Devprayag in Tehri Garhwal district in Uttarakhand, India. Further authentication was obtained from the Botanical Survey of India located in Dehradun, Uttarakhand, with the assigned accession number 116608. To synthesize TiO<sub>2</sub>, titanium isopropoxide (Sigma Aldrich) was used as a precursor. Biochemical characterization kits KB003 and KB009 were utilized for the biochemical tests of isolates. Muller Hilton agar and Nutrient broth (Central Drug House) were used as culture mediums.

#### 2.1.1. Material characterization.

To analyze the crystal structure and phase identification of TiO<sub>2</sub>, a Bruker AXS D8-Advanced diffractometer equipped with CuK $\alpha$ 1 radiation source of wavelength 1.540 Å was utilized. XRD patterns were observed in the 20° to 80° range with a step size of 0.02. Microstructural analysis was conducted on the specimens using a Carl Zeiss Ultra plus Field-Emission Scanning Electron Microscope operated at an accelerated voltage of 15.00 Kv. FTIR analysis was used in particle range 400 to 4000 cm<sup>-1</sup>. Cary 5000 UV-Vis-NIR Spectrophotometer observed the optical properties of synthesized nanoparticles.

#### 2.2. Isolation of bacteria.

##### 2.2.1. Sample collection.

The specimens were collected from 10 different patients with wound infections from City Hospital, Haridwar. Collected specimens were kept in an ice pack for further processing. The pour plate technique was employed to screen bacterial isolates on nutrient agar plates, which were subsequently subjected to incubation at 37°C for 24 hours.

##### 2.2.2. Biochemical characterization.

Biochemical characterization of all the isolates was done using KB009 TM HiCarbo Kit (KB009A / KB009B1 / KB009C) and KB003 TM Hi25 *Enterobacteriaceae* Identification Kits produced by HiMedia Laboratories. Both kits cover 45 biochemical tests, including major tests for biochemical characterization. Biochemical tests are based on substrate utilization and changes in pH. Upon incubation test, organisms undergo metabolic changes confirmed by the change in color of the media, which is likewise visible spontaneously or by adding a reagent.

#### 2.3. Molecular characterization.

##### 2.3.1. DNA extraction.

The isolation of genomic DNA from isolated bacteria was carried out by the cetyltrimethylammonium bromide) CTAB method as described by Wilson [15]. 5 ml of a broth culture of isolated bacterial strains was centrifuged for 2 min. Pellets that were formed by centrifugation were retained, and supernatants were discarded. To achieve a concentration of 100 µg/ml of proteinase K in 0.5% sodium dodecyl sulfate, the pellets were mixed with 567 µl

of T.E. (Tris-EDTA) buffer and supplemented with 10% sodium dodecyl sulfate (SDS) and 30  $\mu$ l of proteinase K (20 mg/ml). The resulting mixture was then incubated at 37°C for 1 hour. After the incubation, 5 M NaCl was added to each sample at the concentration of 100  $\mu$ l. Afterward, 80  $\mu$ l of CTAB/NaCl solution was introduced and left to incubate at 65°C for 10 minutes. After the incubation, 0.7 ml of chloroform/isoamyl alcohol in the ratio 2:1 was added, and the samples were subjected to centrifuge again for 5 min. The supernatant was collected in the fresh vial, and phenol/chloroform/isoamyl alcohol was added in the ratio of 25:25:1. Whole solution was centrifuged for 5 min. The supernatant was again transferred to a fresh vial, and 0.6 ml of isopropanol was added to precipitate nucleic acids. Vials were vortex until the DNA precipitate was visible. DNA pellets were transferred to the fresh tube containing 70% ethanol, followed by heat sealing under a Bunsen burner. DNA samples were washed with 70% ethanol by repetitive centrifugation for 5 min each cycle, and the supernatant was discarded. Pellets were dried by lyophilization and re-dissolved in 100  $\mu$ l of T.E. buffer.

### 2.3.2. 16S rRNA gene amplification.

The amplification of the 16S rRNA gene required the universal primers 27F (5'-AGAGTTTGATCMTGGCTCAG3') and 1492R (5'TACGGYTACCTTGTTACGACTT3') was employed. 0.1 $\mu$ M of each primer was mixed in the reaction mixture that contains 5  $\mu$ l of 10X buffer, 1.5 mM MgCl<sub>2</sub>, 200  $\mu$ M dNTPs (deoxyribonucleotide triphosphate), 2.5U Taq polymerase, and 20 -40 ng template DNA making the volume of 35  $\mu$ l.

The following conditions were provided for PCR: the process began with an initial denaturation at 94°C for 2 minutes, followed by 35 cycles consisting of 1 minute at 94°C, 1.5 minutes at 55°C, and 1 minute at 72°C. A final extension was then performed at 72°C for 3 minutes. The PCR product formed after the reaction was visualized on 1% agarose gel after staining with EtBr (Ethidium Bromide) under UV light [16].

### 2.3.3. 16S rRNA gene sequencing and phylogenetic analysis.

The purified microbial gene fragments were sequenced at Macrogen, Inc., South Korea. Sequencing was accomplished using an automated sequencer 23 ABI 3730XLs works on the principle of Sanger sequencing. Sequencing primers 785F 5' (GGA TTA GAT ACC CTG GTA) 3' as forward and 907R 5' (CCG TCA ATT CMT TTR AGT TT) 3' as reverse were used for the analysis. The sequences that were acquired underwent a BLAST analysis (Basic Local Alignment Search Tool) to compare them with the NCBI database. After submitting the sequences to the NCBI database, an accession number was generated for each sequence. Afterward, the neighbor-joining method used MEGA software to construct phylogenetic trees from the evolutionary distances.

### 2.3.4. Extraction of plant extract.

After drying in the shade for 15-16 days, the leaves of the plant were ground into a coarse powder, and 200 g of the powder was placed in a Soxhlet apparatus for extraction with four different solvents: petroleum ether, benzene, methanol, and water [17].

### 2.3.5. Antimicrobial activity.

The turbidity was adjusted to McFarland standards of 0.5 in nutrient broth to prepare the bacterial inoculum for antibacterial activity. The well diffusion method was used to measure the antibacterial activities of the samples. Four wells of 6 mm diameter were punched by sterile cork borer on Muller Hilton agar plates and further seeded with stock bacterial cultures [18]. Distilled water was used to disperse the powdered nanoparticle composites to a 50 µg/ml concentration. The resulting mixture was exposed to UV light for an hour, and 45 µl of each sample was added to the wells. As positive controls, antibiotic disks of cefazolin (30 mcg), streptomycin (10 mcg), and ampicillin (10 mcg) were used, while distilled water was used as the negative control. All the plates were tested in triplicates and incubated at 37°C for 24 hours. The results were recorded by means of the zone of inhibition in mm.

## 3. Results and Discussion

### 3.1. Structural and morphological studies.

The X-ray diffraction (XRD) pattern for four different samples, namely TiO<sub>2</sub>/PE, TiO<sub>2</sub>/BZ, TiO<sub>2</sub>/M, and TiO<sub>2</sub>/W, was analyzed. The XRD peaks observed corresponded to the anatase phase of TiO<sub>2</sub>, which was confirmed by comparison to JCPDS card no. 21-1272. (Figure 1) shows that an increase in peak width indicates a decrease in particle size. Using the Scherer formula, the average crystallite size of the particles was calculated and reported in nanometers.

$$d = \frac{0.9\lambda}{\beta \cos\theta} \quad (1)$$

The formula used to calculate the mean diameter of the particles involves several parameters:

The parameter '*d*' denotes the average diameter of the particles, '*λ*' refers to the wavelength of radiation, '*β*' represents the angular full width at half maximum (FWHM) of the peak, and '*θ*' signifies the diffraction angle. In the XRD pattern analysis of chemically synthesized TiO<sub>2</sub> and TiO<sub>2</sub>/plant extract composites, reflections on 101, 004, 200, 211, 204, and 215 were observed, indicating the presence of the anatase phase. The average crystallite sizes of TiO<sub>2</sub> composites with petroleum ether extract, benzene extract, methanol extract, and water in four different extracts were found to be in the range of 17-30 nm, 21-33 nm, 19-29 nm, and 7-15 nm, respectively (Figure 1).

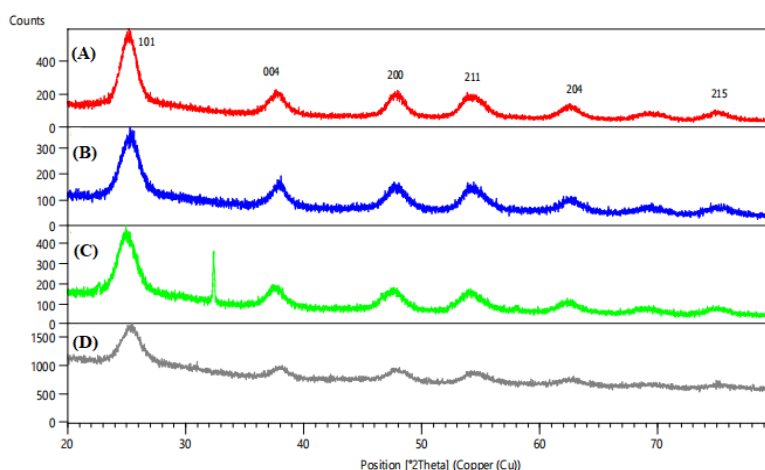


**Figure 1.** XRD pattern (a) TiO<sub>2</sub>/PE; (b) TiO<sub>2</sub>/BZ; (c) TiO<sub>2</sub>/M; (d) TiO<sub>2</sub>/W.

Figure 2 displays the surface characteristics of the samples that were examined using field-emission scanning electron microscopy (FESEM). Specifically, Figure 2(a) corresponds to TiO<sub>2</sub>/PE, 2(b) to TiO<sub>2</sub>/BZ, 2(c) to TiO<sub>2</sub>/M, and 2(d) to TiO<sub>2</sub>/W. Upon magnification of 100 nm, spherical-shaped particles in agglomerated form were observed. The agglomeration phenomenon is caused by the particles' elevated surface energy and the Van der Waals attractive forces between them. Thus, the particles agglomerate in order to reduce their surface energy, as previously reported by Gosens *et al.* [19]. The average grain size of the particles, as determined by Image J software, was found to be 15-30 nm. These results are in agreement with those obtained through XRD analysis.

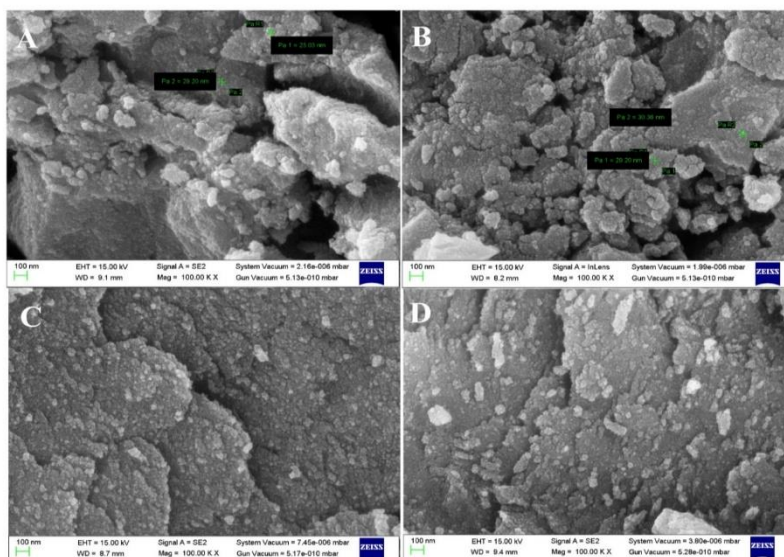


**Figure 2.** FESEM images of (a) TiO<sub>2</sub>/PE; (b) TiO<sub>2</sub>/BZ; (c) TiO<sub>2</sub>/M; (d) TiO<sub>2</sub>/W.

### 3.2. FTIR analysis.

FTIR images of green synthesized TiO<sub>2</sub> were displayed in Figure 3 (a) TiO<sub>2</sub>/PE, (b) TiO<sub>2</sub>/BZ, (c) TiO<sub>2</sub>/M, and (d) TiO<sub>2</sub>/W. During FTIR analysis, the bands were observed at 3700 cm<sup>-1</sup>, 3600 cm<sup>-1</sup>, 3603 cm<sup>-1</sup>, 3595 cm<sup>-1</sup>, 3590 cm<sup>-1</sup>, and 3273 cm<sup>-1</sup>, which shows strong OH stretching vibrations. Weak bonds of OH stretching were observed at 3190 cm<sup>-1</sup>, 3192 cm<sup>-1</sup> and 3050 cm<sup>-1</sup>. The band observed at 2928 cm<sup>-1</sup> corresponds to C-H stretching, and at 2853 cm<sup>-1</sup>, CH<sub>2</sub> and 2727 cm<sup>-1</sup> show N-H stretching. H-bonded NH vibrations were observed at 2600 cm<sup>-1</sup>. The band observed at 2190 cm<sup>-1</sup> and 2140 cm<sup>-1</sup> corresponds to weak C≡C stretching. A combination of hindered rotation and OH bending was observed at 2100 cm<sup>-1</sup>. The origin of vibrational bands at 1997 cm<sup>-1</sup> and 1953 cm<sup>-1</sup> shows the bands corresponding to the 2<sup>nd</sup> order. At 1736 cm<sup>-1</sup>, C=O stretching was observed [20, 21]. The vibrational band at 1636 cm<sup>-1</sup> corresponds to the bending modes of TiOH [22]. The band at 1592 cm<sup>-1</sup> corresponds to C=N, whereas 1517 cm<sup>-1</sup> corresponds to the vibrational band of amide. The vibrational band at 1430 cm<sup>-1</sup> corresponds to CH<sub>2</sub>, deformation of NH was observed at 1412 cm<sup>-1</sup>, and asymmetric stretching of the phosphate group was observed at 1224 cm<sup>-1</sup>. At 1156 cm<sup>-1</sup>, C-O stretching was observed; 1145 cm<sup>-1</sup> corresponds to C-OH. Vibrational absorption of Ti-O-Ti linkage was observed at 1000 cm<sup>-1</sup> - 500 cm<sup>-1</sup> [23] (Figure 3).

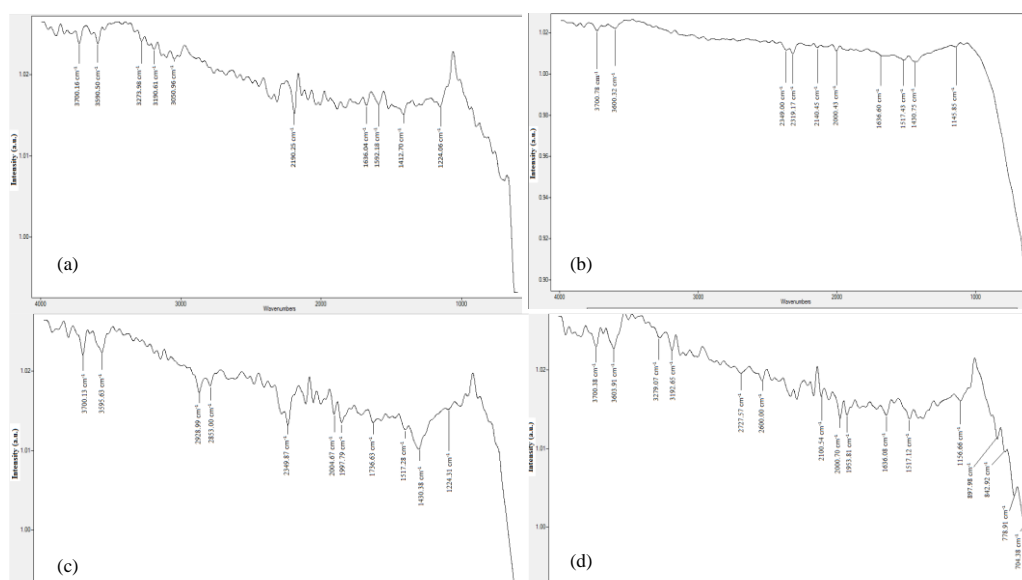


**Figure 3.** FTIR Image of green synthesized TiO<sub>2</sub> (a) TiO<sub>2</sub>/PE; (b) TiO<sub>2</sub>/BZ; (c) TiO<sub>2</sub>/M; (d) TiO<sub>2</sub>/W.

### 3.3. UV-Visible analysis of nanoparticles.

The optical property of synthesized nanoparticles was observed by UV visible spectroscopy. The following equation analyzed the band energy of synthesized nanoparticles:

$$E_g = 1239.8/\lambda \quad (2)$$

Where  $E_g$  = Bandgap (eV),  $\lambda$  = Wavelength (nm).

The absorption spectrum peaks were observed around 319-360 nm wavelength. The U.V. absorption measurement showed the band absorption of TiO<sub>2</sub>-P.E. at 3.4 eV, TiO<sub>2</sub>-BZ at 3.6 eV, TiO<sub>2</sub>-MeOH at 3.8 eV, and TiO<sub>2</sub>- W showed bandgap 3.6 eV. The absorption spectrum depicts a hypsochromic shift. This blue shift is attributed to a decrease in crystallite size [24] (Figure 4).

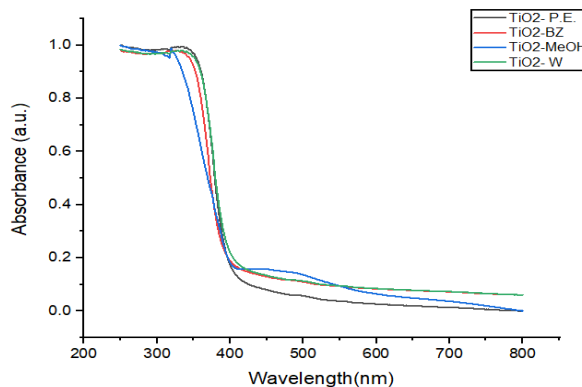


**Figure 4.** U.V. Visible spectra of green synthesized TiO<sub>2</sub> (a) TiO<sub>2</sub>/PE; (b) TiO<sub>2</sub>/BZ; (c) TiO<sub>2</sub>/M; (d) TiO<sub>2</sub>/W.

### 3.4. Bacterial morphological and biochemical studies.

The microbes isolated from the patients having wound infection were screened based on their growth, and the five best-grown cultures were labeled as Isolate B, Isolate C, isolate D, Isolate E, and Isolate G. The Gram's staining technique was used to characterize the isolates (Figure 5) morphologically. Table 1 shows the evaluation of Gram's staining results of isolated bacteria. Isolate B, Isolate C, and Isolate D showed spherical morphology. They appeared in spherical bunches and retained a purple color. Isolates E and G appeared to be rod-shaped and retained a pink color. Based on morphological characterization, Isolates B, C, and D were

Gram's positive cocci, and isolates E and G were Gram's negative rods. Figure 5 shows the morphology of the isolated bacteria (a) Isolate B (b) Isolate C (c) Isolate D (d) Isolate E (e) Isolate G. Table 2 shows the results of 46 biochemical tests of isolated bacteria, which includes 45 biochemical test results from both the kits (KB003 and KB009) and the catalase test was performed separately.

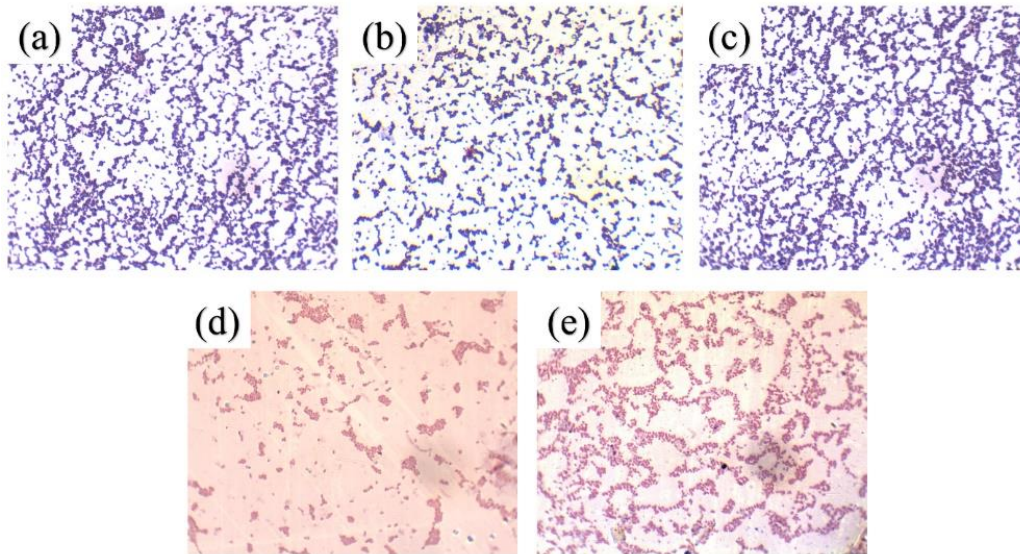


**Figure 5.** Morphology of the isolated bacteria (Magnification -1000X) (a) Isolate B, Gram-positive cocci; (b) Isolate C, Gram-positive cocci; (c) Isolate D, Gram-positive cocci; (d) Isolate E, Gram-negative rods; (e) Isolate G, Gram-negative rods.

**Table 1.** Morphological characteristics of the isolates.

S. No.	Isolates	Morphology	Grams staining
1	Isolate B	Spherical	Gram-positive
2	Isolate C	Spherical	Gram-positive
3	Isolate D	Spherical	Gram-positive
4	Isolate E	Rod-shaped	Gram-negative
5	Isolate G	Rod-shaped	Gram-negative

**Table 2.** Biochemical characterization of isolated bacteria.

S. No.	Biochemical tests	Isolate B	Isolate C	Isolate D	Isolate E	Isolate G
1	ONPG	-	-	-	-	-
2	Citrate utilization	+	+	+	+	+
3	Lysin utilization	+	+	+	-	+
4	Methyl red	-	-	-	-	+
5	Voges Proskauer	+	+	+	-	+
6	Nitrate reduction	+	+	+	+	+
7	Indole	-	-	-	-	-
8	Oxidase	-	-	-	+	-
9	Catalase	+	+	+	+	+
10	H <sub>2</sub> S production	-	-	-	-	-
11	Lactose	-	-	-	-	+
12	Xylose	-	-	-	-	+
13	Maltose	-	-	-	+	+
14	Fructose	+	+	+	+	+
15	Dextrose	+	+	+	+	+
16	Galactose	-	-	-	+	+
17	Raffinose	-	-	-	-	-
18	Trehalose	+	+	+	+	+
19	Melibiose	-	-	-	+	+
20	Sucrose	+	+	+	+	+
21	L- Arabinose	-	-	-	-	+
22	Mannose	-	-	-	+	-
23	Inulin	-	-	-	-	-
24	Sodium gluconate	-	-	-	-	+
25	Glycerol	-	-	-	+	+

S. No.	Biochemical tests	Isolate B	Isolate C	Isolate D	Isolate E	Isolate G
26	Salicin	-	-	-	-	+
27	Dulcitol	-	-	-	-	-
28	Inositol	-	-	-	-	-
29	Sorbitol	-	-	-	-	-
30	Mannitol	-	-	-	+	-
31	Adonotol	-	-	-	-	-
32	Erythritol	-	-	-	-	-
33	$\alpha$ -Methyl-D-glucoside	-	-	-	-	-
34	Rhamnose	-	-	-	-	+
35	Cellobiose	-	-	-	+	-
36	Melezitose	-	-	-	+	-
37	$\alpha$ -Methyl-D- Mannoside	-	-	-	-	-
38	Esculin	+	+	+	+	+
39	D-Arabinose	-	-	-	-	+
40	Malonate	-	-	-	-	-
41	Sorbose	-	-	-	-	-
42	Ornithine utilization	+	+	+	+	+
43	Phenylalanine deamination	-	-	-	-	-
44	Saccharose utilization	+	+	+	+	+
45	Arabitol utilization	-	-	-	-	-
46	Glucose utilization	-	-	-	-	-

### 3.5. Molecular studies.

Molecular characterization of the isolated bacteria was done by 16S rRNA sequencing. In this scenario, the genome of isolates was amplified by universal primers:

27F (5'- AGAGTTTGATCMTGGCTCAG3') for forward.

1492 R (5'TACGGYTACCTTGTTACGACTT3') for reverse.

16S rRNA gene amplicons of “Isolate B, Isolate C, Isolate D, Isolate E, and Isolate G” were subjected to sequencing to identify up to species level. On Comparison with sequences in the NCBI public database using BLAST search accession no. MK503460 for Isolate B, MK503462 for Isolate C, MK503463 for Isolate D, MK503459 for Isolate E, and MK765005 for Isolate G were allotted.

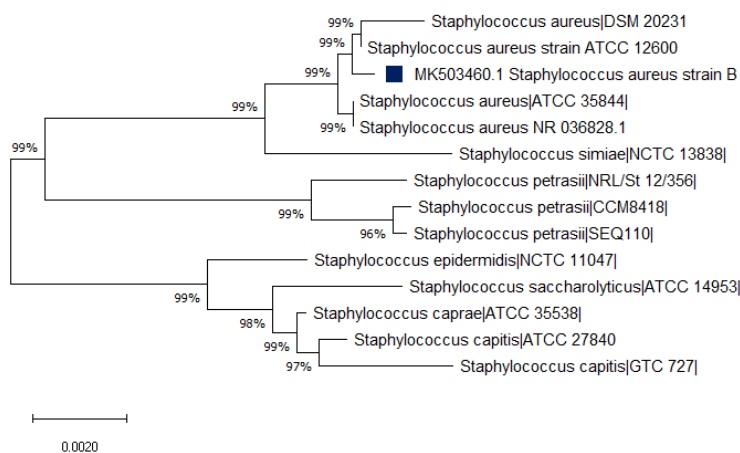


**Figure 6.** *Staphylococcus aureus* strain B 16S ribosomal RNA gene, partial sequence, and neighbor-joining tree based on 16S ribosomal RNA sequence showing the relationship between Isolate B and its closely related species.

NCBI-BLAST results identified Isolate B, C, and D as *Staphylococcus aureus* (Staphylococcaceae) with 99% similarity, Isolate E as *Pseudomonas aeruginosa* (Pseudomonadaceae) with 99%, and Isolate G as *Escherichia coli* (Enterobacteriaceae) with 99%. Isolate B and Isolate C were closely related to *Staphylococcus aureus* strain ATCC

12600, having accession no. NR\_115606 and *S. aureus* strain NBRC\_100910, having accession no. NR\_113956 (Figures 6 and 7). Isolate D was closely related to *S. aureus* strain DSM 2031 (Figure 8). Isolate E was closely related to *P. aeruginosa* strain JCM 5962 (Figure 9). Isolate G was closely related to *E. coli* strain ATCC 1175 (Figure 10).

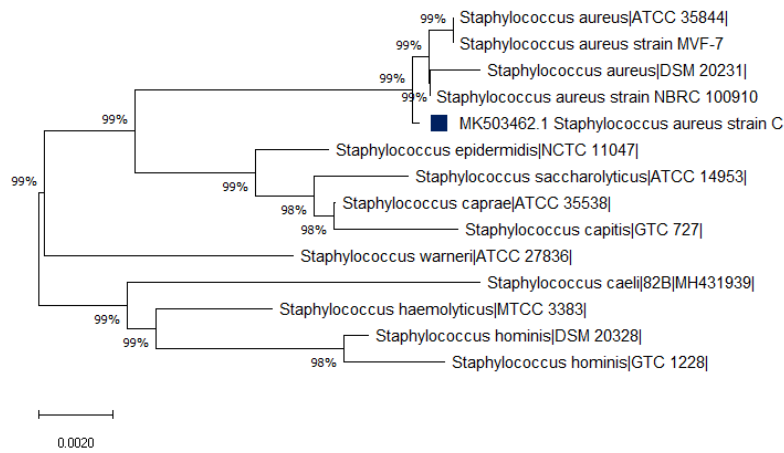


**Figure 7.** *Staphylococcus aureus* strain C 16S ribosomal RNA gene, partial sequence, and neighbor-joining tree based on 16S ribosomal RNA sequence showing the relationship between Isolate C and its closely related species.

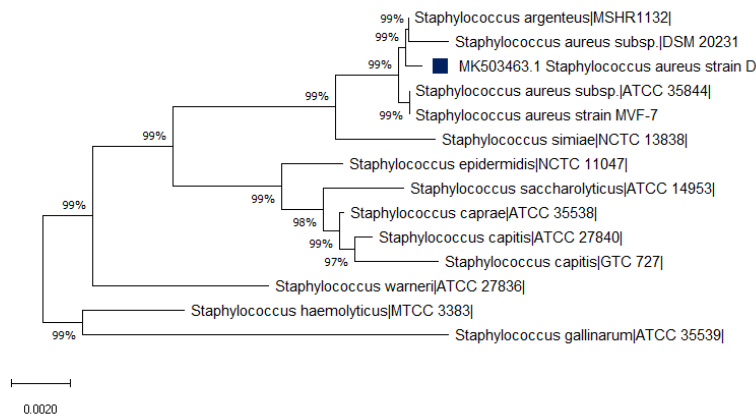


**Figure 8.** *Staphylococcus aureus* strain D 16S ribosomal RNA gene, partial sequence, and neighbor-joining tree based on 16S ribosomal RNA sequence showing the relationship between Isolate D and its closely related species.

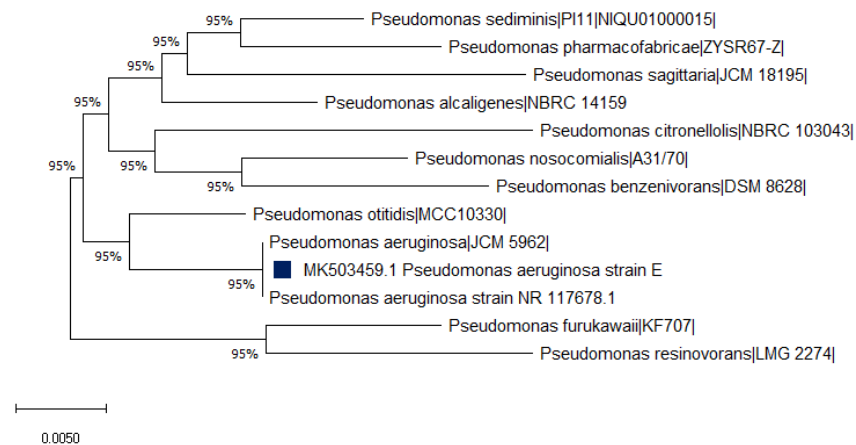


**Figure 9.** *Pseudomonas aeruginosa* strain E 16S ribosomal RNA gene, partial sequence, and neighbor-joining tree based on 16S ribosomal RNA sequence showing the relationship between Isolate E and its closely related species.

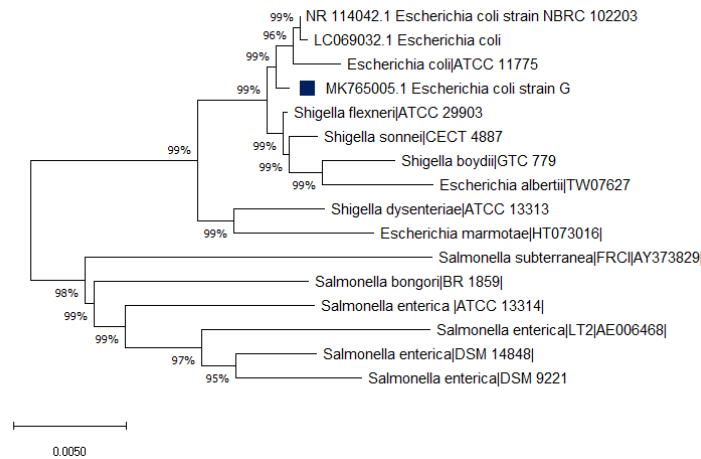


**Figure 10.** *Escherichia coli* strain G 16S ribosomal RNA gene, partial sequence, and neighbor-joining tree based on 16S ribosomal RNA sequence showing the relationship between Isolate G and its closely related species.

### 3.6. Antibacterial activity.

The TiO<sub>2</sub>/PE nanoparticles among the isolates gave maximum zone of inhibition against *Pseudomonas aeruginosa* strain E (23.66±0.88 mm) followed by *Staphylococcus aureus* strain D (19.66±0.33 mm), *Staphylococcus aureus* strain B (14.00±0.00 mm), *Staphylococcus aureus* strain C (12.33±0.66 mm) and *Escherichia coli* strain G (09.33±0.33 mm). TiO<sub>2</sub>/BZ nanoparticles gave maximum inhibition against *Pseudomonas aeruginosa* strain E (17.66±0.88 mm), followed by *Staphylococcus aureus* strain C (10.33±0.66 mm), *Staphylococcus aureus* strain B, D and *Escherichia coli* strain G (10.00±0.00 mm). The maximum inhibition was noticed for TiO<sub>2</sub>/MeOH nanoparticles against *Pseudomonas aeruginosa* strain E (19.33±0.88 mm) followed by *Staphylococcus aureus* strain D (15.00±0.00 mm), *Staphylococcus aureus* strain B (13.00±0.00 mm), *Staphylococcus aureus* strain C and *Escherichia coli* strain G (12.00±0.00 mm). The TiO<sub>2</sub>/W nanoparticles gave maximum antibacterial potential against *Pseudomonas aeruginosa* strain E (21.00±0.00 mm) followed by *Staphylococcus aureus* strain D (11.66±0.33 mm), *Staphylococcus aureus* strain B (11.00±0.00 mm), *Staphylococcus aureus* strain C (10.33±0.33 mm) and *Escherichia coli* strain G (10.00±0.00 mm) The statistically significant differences in the different zone of inhibitions for each treatment was determined by the ANOVA test. The results reveal an F-value of 7.8009 and a p-value of 0.0000539, indicating the significant differences between the treatments (Table 3) (Figures 11-13).

**Table 3.** Zone of inhibition(diameter in mm) for different isolates and treatments.

S. No.	Zone of inhibition (diameter in mm)							
	TiO <sub>2</sub> / PE	TiO <sub>2</sub> / BZ	TiO <sub>2</sub> / M	TiO <sub>2</sub> / W	DW	Amp	Cfz	Str
<b>B</b>	14.00±0.00	10.00±0.00	13.00±0.00	11.00±0.00	-	08.00±0.00	12.66±0.33	17.00±0.57
<b>C</b>	12.33±0.66	10.33±0.66	12.00±0.00	10.33±0.33	-	10.00±0.00	15.00±0.00	25.33±0.33
<b>D</b>	19.66±0.33	10.00±0.00	15.00±0.00	11.66±0.33	-	09.66±0.33	15.66±0.33	24.33±0.33
<b>E</b>	23.66±0.88	17.66±0.88	19.33±0.88	21.00±0.00	-	08.00±0.00	08.00±0.00	24.33±0.88
<b>G</b>	09.33±0.33	10.00±0.00	12.00±0.00	10.00±0.00	-	07.00±0.00	09.66±0.33	30.00±0.00

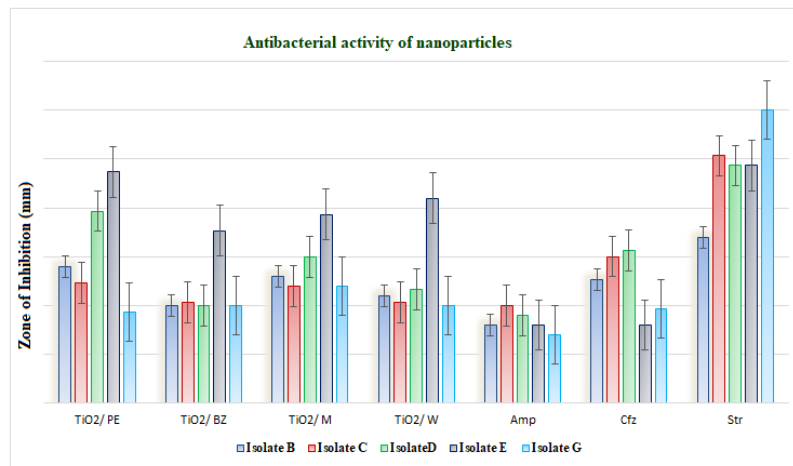


**Figure 11.** The graphical representation shows the comparison of the zone of inhibition between antimicrobial agents used against isolated pathogens from wounds, i.e., (a) *Staphylococcus aureus* strain B; (b) *Staphylococcus aureus* strain C; (c) *Staphylococcus aureus* strain D; (d) *Pseudomonas aeruginosa* strain E; (e) *Escherichia coli* G.

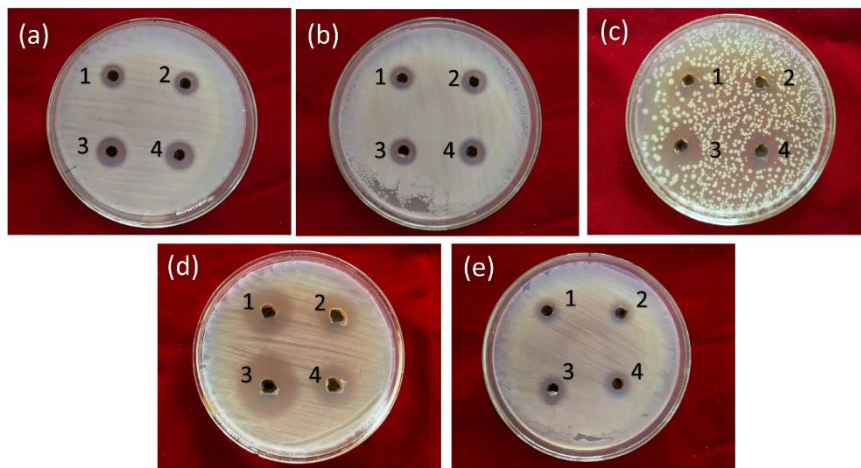


**Figure 11.** The antibacterial screening of *Leucas indica* aerial parts extracts nanoparticles (1. Benzene, 2. Water, 3. Petroleum ether, and 4. Methanol) against isolated pathogens from wounds, i.e., (a) *Staphylococcus aureus* strain B; (b) *Staphylococcus aureus* strain C; (c) *Staphylococcus aureus* strain D; (d) *Pseudomonas aeruginosa* strain E; (e) *Escherichia coli* G.

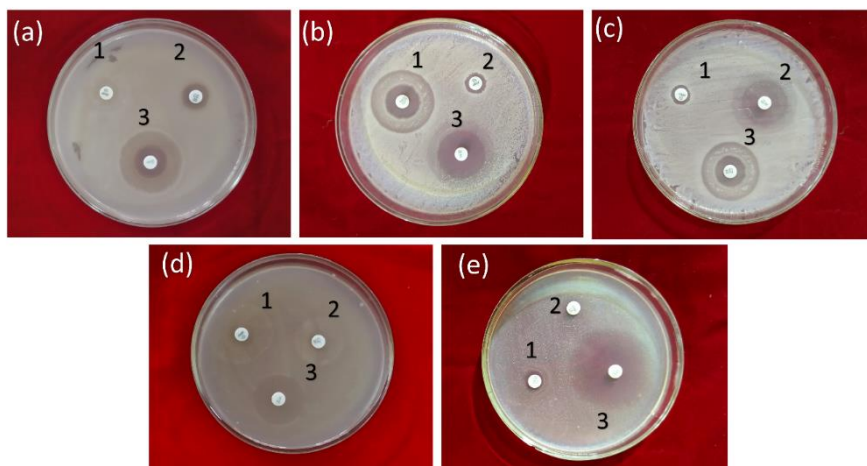


**Figure 12.** The antibacterial screening of positive control (1. Cefazolin (30 mcg), 2. Ampicillin (10 mcg), and Streptomycin (10 mcg)) against isolated pathogens from the wound, i.e. (a) *Staphylococcus aureus* strain B; (b) *Staphylococcus aureus* strain C; (c) *Staphylococcus aureus* strain D; (d) *Pseudomonas aeruginosa* strain E; (e) *Escherichia coli* G.

The general mechanism of the sol-gel process employs the network formation of oxides through the condensation reaction between the reactant and precursor in the liquid medium. Process accompanying several stages starting right from the colloidal solution of precursor and reactant typically known as “sol”. Sol gradually turns into a more or less diphasic (liquid and solid) gel-like substance, which is further transformed into gel [25]. It is a process in which low temperature is utilized to obtain better results. Among the molecular precursors, metal alkoxides are more adaptable precursors for synthesizing metal oxides. Metal oxides are usually synthesized by hydrolysis, condensation, and polycondensing of the metal alkoxides. Livage proposed an acceptable reaction mechanism (1988) [26].

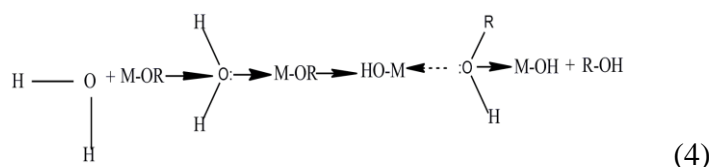
The overall reaction is written as:



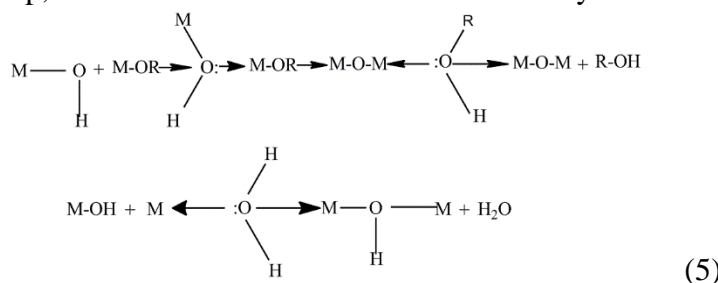
Due to the high electro-negativity of alkoxy groups (OR), metal atoms undergo nucleophilic substitution reactions. Therefore, metal alkoxides are highly reactive with water, resulting in the formation of hydroxides.

### 3.7. Reaction mechanism.

In the first step, the nucleophilic addition of water molecules to the positively charged metal atom occurs, which results in the substitution of the alkoxy group with the hydroxyl group.



In the second step, a condensation reaction forms oxo and hydroxo bridges.



Here, both the reactions are quick and somehow have the same reaction rates. Hydrolysis and condensation rates and the structure of the product can be influenced by acid catalysts.

The antimicrobial efficacy of the synthesized nanoparticles was tested against 5 isolated bacteria (*Staphylococcus aureus* strain B, C, D, *Pseudomonas aeruginosa* strain E, and *Escherichia coli* strain G) from the patients suffering from the infection of the wound. Here, we found that all the tested nanoparticles were surprisingly best at their antimicrobial efficacy against all the isolates, even though most gave better results than antibiotics used as the positive control. The isolated *Pseudomonas aeruginosa* Strain E was most sensitive against all the synthesized nanoparticles, even though it gave better antimicrobial potential than ampicillin and cefazoline. Similarly, isolated *Staphylococcus aureus* strains B, C, and D are also sensitive to the synthesized samples. On the other hand, isolated *Escherichia coli* strain G was found to be the least sensitive. Overall, titanium dioxide synthesized from petroleum ether extract gave the best antimicrobial efficacy against all the test organisms except *Escherichia coli* strain G.

The nanoparticles utilized for the antimicrobial efficacy were in the anatase phase. The bandgap of the anatase phase of TiO<sub>2</sub> nanoparticles is 3.2 eV and has been found to be the most active form. Its photocatalytic process produces reactive species that are fatal to the microbes [27]. When titanium dioxide particles are attached to the surface of a cell, there is a possibility of direct transfer of electrons between the organism and the particles. Even very small particles of titanium dioxide can enter the cell and facilitate electron transfer within the cell. However, light is essential for photocatalysis as it may cause direct photochemistry from any ultraviolet source. Photochemistry may also be enhanced by irradiation on microbes while adsorbed to oxide surfaces [28]. Hence, prior to the antimicrobial activity testing, the synthesized nanoparticles underwent ultraviolet radiation irradiation. The antibacterial properties of the nanoparticles may stem from the reaction between reactive oxygen species (ROS) and lipid membranes, resulting in the peroxidation of lipids and ultimately leading to the rupture of the cell membrane and cell death. ROS generation may be because of the efficiency in the production of OH in the anatase phase of TiO<sub>2</sub> nanoparticles [29-30]. Upon interacting with the cell, the anatase phase of TiO<sub>2</sub> nanoparticles produces OH radicals, which are highly reactive, which is why they are short-lived. At the moment of their generation, they immediately interact with the outer surface of the bacteria until the titanium dioxide particles penetrate the cell [27]. Figure (14) shows the schematic representation of the cell damage due to ROS. Cell damage by the nanoparticles can be summarized by the following steps:

The production of reactive oxygen species by the titanium dioxide nanoparticles induces the electron-hole pair under the radiation.

The nanoparticle's large surface area generates an electrostatic force that allows it to attach to the surface of bacteria cells, ultimately leading to peroxidation and damage to the cell.

As the cell wall gets damaged, cytoplasm flows out, helping nanoparticles to enter inside the cell following the damage to the cell organelles [31].

The present study's significance lies in the extensive exploitation of antibiotics, which has led to several drug-resistant bacteria causing delayed healing or much worse circumstances. So, there is a need to develop certain novel kinds of medications under such conditions. The current study focuses on preparing an alternative medication or compound that can be used with conventional medicine against wound infection-causing pathogens.

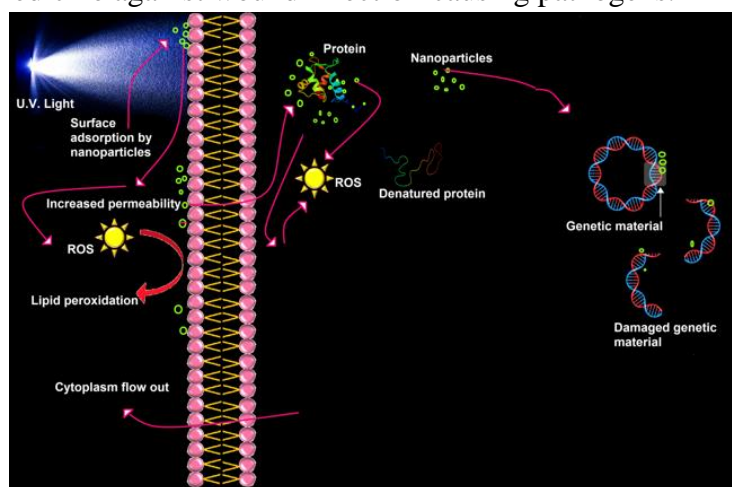


**Figure 13.** The image shows the damage to cells caused by the TiO<sub>2</sub> nanoparticles via (ROS). This ROS generation triggers the electron-hole pair under UV radiation. An electrostatic force is exerted by the large surface area of the nanoparticles, enabling them to attach to the bacterial cell surfaces, leading to peroxidation and cell damage (*Image courtesy: Author*).

## 4. Conclusion

In the present study, titanium dioxide nanoparticles were successfully synthesized by using the crude extract of the herb *Leucas indica*. When subjected to the antibacterial activity against isolated bacteria from the wound infection site, these green synthesized nanoparticles gave potential results. This green synthetic approach is eco-friendly, economical, and cost-effective. As far as its antimicrobial potential and drug delivery properties are concerned, it can be utilized as one of the constituents of conventional topical ointments against skin and wound infection pathogens.

## Funding

The authors gratefully acknowledge Rajiv Gandhi National Fellowship (F1-17.1/2017-18/RGNF-2017-18-SC-UTT-28508) for the financial support and Gurukula Kangri (Deemed to be University), Haridwar, for providing the lab facility to carry out this research work.

## Acknowledgments

The authors sincerely acknowledge the technical support provided by IIT Roorkee for completing the research work.

## Conflicts of Interest

The authors declare no conflict of interest.

## References

1. Ahmed, R. M.; Hasan, I. A review on properties and applications of TiO<sub>2</sub> and associated nanocomposite materials. *Materials Today: Proceedings* **2023**, *81*, 1073-1078, <https://doi.org/10.1016/j.matpr.2021.04.381>.
2. Li, D.; Song, H.; Meng, X.; Shen, T.; Sun, J.; Han, W.; Wang, X. Effects of particle size on the structure and photocatalytic performance by alkali-treated TiO<sub>2</sub>. *Nanomaterials* **2020**, *10*, 546, <https://doi.org/10.3390/nano10030546>.
3. Arun, J.; Nachiappan, S.; Rangarajan, G. *et al.* Synthesis and application of titanium dioxide photocatalysis for energy, decontamination and viral disinfection: a review. *Environ. Chem. Lett.* **2023**, *21*, 339–362, <https://doi.org/10.1007/s10311-022-01503-z>.
4. Berardinelli, A.; Parisi, F. 11 - TiO<sub>2</sub> in the food industry and cosmetics. In *Titanium Dioxide (TiO<sub>2</sub>) and Its Applications*, Parrino, F., Palmisano, L., Eds.; Elsevier: **2021**; pp. 353-371, <https://doi.org/10.1016/B978-0-12-819960-2.00008-0>.
5. Reghunath, S.; Pinheiro, D.; KR, S. D. A review of hierarchical nanostructures of TiO<sub>2</sub>: Advances and applications. *Applied Surface Science Advances* **2021**, *3*, 100063, <https://doi.org/10.1016/j.apsadv.2021.100063>.
6. Musial, J.; Krakowiak, R.; Mlynarczyk, D. T.; Goslinski, T.; Stanisz, B. J. Titanium dioxide nanoparticles in food and personal care products—What do we know about their safety?. *Nanomaterials* **2020**, *10*, 1110, <https://doi.org/10.3390/nano10061110>.
7. Ayorinde, T.; Sayes, C. M. An Updated Review of Industrially Relevant Titanium Dioxide and its Environmental Health Effects. *Journal of Hazardous Materials Letters* **2023**, *4*, 100085, <https://doi.org/10.1016/j.hazl.2023.100085>.
8. Sharma, D.; Kanchi, S.; Bisetty, K. Biogenic synthesis of nanoparticles: a review. *Arabian journal of chemistry* **2019**, *12*, 3576-3600, <https://doi.org/10.1016/j.arabjc.2015.11.002>.
9. Babu, N.; Pathak, V. M.; Singh, A.; Navneet, A. Sonchus asper leaves aqueous extract mediated synthesis of Titanium dioxide nanoparticles. *Pharma Innov. J.* **2019**, *8*, 817-822.

10. Bokov, D.; Turki Jalil, A.; Chupradit, S.; Suksatan, W.; Javed Ansari, M.; Shewael, I. H.; Kianfar, E. Nanomaterial by sol-gel method: synthesis and application. *Advances in Materials Science and Engineering* **2021**, *2021*, 1-21, <https://doi.org/10.1155/2021/5102014>.
11. Eslami, A.; Lachini, S. A.; Shaterian, M.; Karami, M.; Enhessari, M. Sol-gel synthesis, characterization, and electrochemical evaluation of magnesium aluminate spinel nanoparticles for high-capacity hydrogen storage. *Journal of Sol-Gel Science and Technology* **2023**, 1-11, <https://doi.org/10.1007/s10971-023-06260-1>.
12. Babu, N.; Singh, A.; Singh, R. Therapeutics potential and pharmacological properties of *Leucas indica*: A review. *The Pharma Innovation* **2018**, *7*, 564-568.
13. Kumar, S.; Singh, N.; Mittal, A.; Kharkwal, H.; Jain, S. K.; Goel, B. The genus *Leucas*: A review on phytochemistry and pharmacological activities. *Fitoterapia* **2023**, *167*, 105492. <https://doi.org/10.1016/j.fitote.2023.105492>.
14. Liu, H.; Yang, W.; Ma, Y.; Cao, Y.; Yao, J.; Zhang, J.; Hu, T. Synthesis and characterization of titania prepared by using a photoassisted sol-gel method. *Langmuir* **2003**, *19*, 3001-3005, <https://doi.org/10.1021/la026600o>.
15. Bogožalec Košir, A.; Lužnik, D.; Tomič, V.; Milavec, M. Evaluation of DNA Extraction Methods for Reliable Quantification of *Acinetobacter baumannii*, *Klebsiella pneumoniae*, and *Pseudomonas aeruginosa*. *Biosensors* **2023**, *13*, 463, <https://doi.org/10.3390/bios13040463>.
16. Gates, L.; Mistry, T.; Ogunbiyi, O.; Kite, K.A.; Klein, N.J.; Sebire, N.J.; Alber, D.G. Identification of bacterial pathogens in sudden unexpected death in infancy and childhood using 16S rRNA gene sequencing. *Frontiers in Microbiology* **2023**, *14*, 1171670, <https://doi.org/10.3389/fmicb.2023.1171670>.
17. Babu, N.; Pathak, V. M.; Singh, A.; Navneet. *Sonchus asper* leaves aqueous extract mediated synthesis of titanium dioxide nanoparticles. *The Pharma Innovation* **2019**, *8(4)*, 817-822
18. Balouiri, M.; Sadiki, M.; Ibensouda, S. K. Methods for in vitro evaluating antimicrobial activity: A review. *Journal of pharmaceutical analysis* **2016**, *6*, 71-79, <https://doi.org/10.1016/j.jpha.2015.11.005>.
19. Vollath, D. Agglomeration of particles stored in a box. *FirePhysChem* **2023**, *3*, 275-280, <https://doi.org/10.1016/j.fpc.2023.03.007>.
20. Movasaghi, Z.; Rehman, S.; ur Rehman, D. I. Fourier transform infrared (FTIR) spectroscopy of biological tissues. *Applied Spectroscopy Reviews* **2008**, *43*, 134-179, <https://doi.org/10.1080/05704920701829043>.
21. Infrared Spectroscopy Absorption Table - Chemistry LibreTexts. Available online: [https://chem.libretexts.org/Ancillary\\_Materials/Reference/Reference\\_Tables/Spectroscopic\\_Parameters/Infrared\\_Spectroscopy\\_Absorption\\_Table](https://chem.libretexts.org/Ancillary_Materials/Reference/Reference_Tables/Spectroscopic_Parameters/Infrared_Spectroscopy_Absorption_Table). Accessed on September, 2020.
22. León, A.; Reuquen, P.; Garín, C.; Segura, R.; Vargas, P.; Zapata, P.; Orihuela, P. A. FTIR and Raman characterization of TiO<sub>2</sub> nanoparticles coated with polyethylene glycol as carrier for 2-methoxyestradiol. *Applied Sciences* **2017**, *7*, 49, <https://doi.org/10.3390/app7010049>.
23. Lu, X.; Lv, X.; Sun, Z.; Zheng, Y. Nanocomposites of poly (L-lactide) and surface-grafted TiO<sub>2</sub> nanoparticles: Synthesis and characterization. *European Polymer Journal* **2008**, *44*, 2476-2481, <https://doi.org/10.1016/j.eurpolymj.2008.06.002>.
24. Zhao, L.; Yu, J. Controlled synthesis of highly dispersed TiO<sub>2</sub> nanoparticles using SBA-15 as hard template. *Journal of Colloid and Interface Science* **2006**, *304*, 84-91, <https://doi.org/10.1016/j.jcis.2006.08.042>.
25. Chang, C.; Rad, S.; Gan, L.; Li, Z.; Dai, J.; Shahab, A. Review of the sol-gel method in preparing nano TiO<sub>2</sub> for advanced oxidation process. *Nanotechnology Reviews* **2023**, *12*, 20230150, <https://doi.org/10.1515/ntrev-2023-0150>.
26. Livage, J.; Henry, M. and Sanchez. C. Sol-gel chemistry of transition metal oxides. *Progress in Solid State Chemistry* **1988**, *18*, 259-351, [http://dx.doi.org/10.1016/0079-6786\(88\)90005-2](http://dx.doi.org/10.1016/0079-6786(88)90005-2).
27. Chakhtouna, H.; Benzeid, H.; Zari, N.; Qaiss, A. E. K.; Bouhfid, R. Recent progress on Ag/TiO<sub>2</sub> photocatalysts: Photocatalytic and bactericidal behaviors. *Environmental Science and Pollution Research* **2021**, *28*, 44638-44666, <https://doi.org/10.1007/s11356-021-14996-y>.
28. Wang, M.; Xu, Z.; Qi, Z.; Cai, Y.; Li, G.; Choi, W.; An, T. Repeated photocatalytic inactivation of *E. coli* by UV+ Ni foam@ TiO<sub>2</sub>: Performance and photocatalyst deactivation. *Chemical Engineering Journal* **2023**, *468*, 143680, <https://doi.org/10.1016/j.cej.2023.143680>.
29. Aflakian, F.; Mirzavi, F.; Aiyelabegan, H. T.; Soleimani, A.; Navashenaq, J. G.; Karimi-Sani, I.; Vakili-Ghartavol, R. Nanoparticles-based therapeutics for the management of bacterial infections: a special emphasis on FDA approved products and clinical trials. *European Journal of Pharmaceutical Sciences* **2023**, *188*, 106515, <https://doi.org/10.1016/j.ejps.2023.106515>.

30. Lee, Y. J.; Jeong, Y. J.; Cho, I. S.; Lee, C. G.; Park, S. J.; Alvarez, P. J. The inhibitory mechanism of humic acids on photocatalytic generation of reactive oxygen species by TiO<sub>2</sub> depends on the crystalline phase. *Chemical Engineering Journal* **2023**, *476*, 146785, <https://doi.org/10.1016/j.cej.2023.146785>.
31. Wang, L.; Hu, C.; Shao, L. The antimicrobial activity of nanoparticles: present situation and prospects for the future. *International journal of nanomedicine* **2017**, *12*, 1227-1249, <https://doi.org/10.2147/IJN.S121956>.